Eur. Phys. J. A **7**, 467–478 (2000)

THE EUROPEAN PHYSICAL JOURNAL A

Consequences of the center–of–mass correction in nuclear mean–field models

M. Bender[1,2,3], K. Rutz[3], P.-G. Reinhard[4,5], J.A. Maruhn[3,5]

[1] Department of Physics and Astronomy, The University of Tennessee, Knoxville, TN 37996, USA
[2] Department of Physics and Astronomy, The University of North Carolina, Chapel Hill, NC 27516, USA
[3] Institut für Theoretische Physik, Universität Frankfurt, Robert–Mayer–Str. 10, 60325 Frankfurt am Main, Germany
[4] Institut für Theoretische Physik II, Universität Erlangen–Nürnberg, Staudtstr. 7, 91058 Erlangen, Germany
[5] Joint Institute for Heavy–Ion Research, Oak Ridge National Laboratory, P.O. Box 2008, Oak Ridge, TN 37831, USA

Received: 6 September 1999
Communicated by P. Schuck

Abstract. We study the influence of the scheme for the correction for spurious center–of–mass motion on the fit of effective interactions for self–consistent nuclear mean–field calculations. We find that interactions with very simple center–of–mass correction have significantly larger surface coefficients than interactions for which the center–of–mass correction was calculated for the actual many–body state during the fit. The reason for that is that the effective interaction has to counteract the wrong trends with nucleon number of all simplified schemes for center–of–mass correction which puts a wrong trend with mass number into the effective interaction itself. The effect becomes clearly visible when looking at the deformation energy of largely deformed systems, e.g. superdeformed states or fission barriers of heavy nuclei.

PACS. 21.60.Jz Hartree-Fock and random-phase approximations – 21.30.Fe Forces in hadronic systems and effective interactions – 21.65.+f Nuclear matter – 24.10.Jv Relativistic models

1 Introduction

It is generally known that the ground–state wave functions of mean–field models break symmetries which had been originally given in the many–body Hamiltonian or effective energy functional. Violation of translational symmetry is unavoidable because the center–of–mass of a system is localised by the mean–field potential. This causes a spurious contribution from the center–of–mass vibrations to the energy and other observables. The problem has been discussed since decades and several solutions have been developed in the course of time, for an overview see [1]. A rigorous way to restore the broken symmetries is the projection method. Projection–before–variation is the perfect solution which has been applied even in realistic applications [2], but it constitutes a numerically extremely challenging task and is still too costly to be used in large–scale investigations of nuclear structure. A simpler approach is the projection–after–variation method where the mere HFB state is varied but projected wave functions are used to calculate observables [1]. A study of this approach in the context of self–consistent models has hinted that full projection effects could be quantitatively important in light nuclei [3]. Nonetheless, by far the most applications deal with approximate ways to compute the center–of–mass corrections for reasons of feasibility and transferability. The standard procedure is to expand the correction in orders of moments $\langle \hat{\mathbf{P}}^{2n}_{\mathrm{c.m.}} \rangle$ and to stop at first order [4]. And even that is often further simplified in various manners. As a consequence there are several recipes around for performing the center–of–mass correction.

This diversity as such could possibly be bearable. The situation is complicated by the fact that all quantitatively successful nuclear mean–field theories employ a phenomenological adjustment of the model parameters [5]. While fitting the parameters one has to decide for one of the current forms of the center–of–mass correction. The first rule to be obeyed is then that all later applications should employ precisely that recipe which had been used during the fit [5], but the influence of the actual recipe goes further than that. The various approximations in themselves do have slightly different trends with mass number. These differences can be counterweighted to a certain extend by slight readjustments within the model parameters relevant for those trends, but the flexibility of the models is limited and systematic differences appear for larger extrapolations, in case of the center–of–mass correction the computation of nuclear–matter properties and finite nuclei at large deformation, e.g. in superdeformed states or fission. It is the aim of this paper to present a thorough investigation of these subtle side effects from the different recipes for the correction for spurious center–of–mass motion which will be simply denoted as c.m. correction in the following. There are, however, several other correc-

tions for spurious motion and broken symmetries to be made, but the c.m. correction is among the most important ones since it is present in all nuclei, while the influence of, e.g. the rotational and vibrational corrections can be suppressed by choosing spherical nuclei with stiff potential energy surfaces. In those, the rotational correction vanishes and the admixture of vibrational excitations to the independent-quasiparticle ground state can be assumed to be negligible.

The paper is outlined as follows: In Sect. 2 we explain briefly the underlying mean–field models in this study. In Sect. 3 we summarise the currently used approximations for the center-of-mass corrections and in Sect. 4, we present and discuss typical observables we find to be sensitive to the treatment of the correction for center-of-mass motion: binding energy systematics and deformation energies. An Appendix presents the formulae needed to calculate the c.m. correction in relativistic and non–relativistic models.

2 Framework

We investigate the c.m. correction in the frameworks of the self–consistent Skyrme–Hartree–Fock (SHF) approach [6] and the relativistic mean–field model (RMF) [7,8]. In both, SHF and RMF, models the corrections for spurious motion can be treated non–relativistically.

The numerical procedure represents the coupled SHF and RMF equations on a grid in coordinate space using a Fourier definition of the derivatives and solves them with the damped gradient iteration method [9]. We consider both spherical and axially symmetric deformed configurations.

Pairing correlations are treated in the BCS scheme using a delta pairing force [10] $\mathrm{V_{pair}} = \mathrm{V_q}\,\delta(\mathbf{r}_1 - \mathbf{r}_2)$. The pairing strengths $\mathrm{V_p}$ for protons and $\mathrm{V_n}$ for neutrons depend on the actual mean–field parametrisation. They are optimised by fitting for each parametrisation separately the pairing gaps from a fourth–order finite–difference formula of binding energies in isotopic and isotonic chains of semi–magic nuclei throughout the chart of nuclei. The pairing–active space is chosen to include the number of one additional shell of oscillator states above the Fermi energy with a smooth Fermi cutoff weight, for details see [11].

3 The center–of–mass correction

The c.m. correction – the change in binding energy from projection–after–variation in first–order approximation – is given by

$$\mathrm{E^{mic}_{c.m.}} = -\frac{1}{2\mathrm{mA}}\langle\hat{\mathbf{P}}^2_{\mathrm{c.m.}}\rangle \quad . \tag{1}$$

We will denote this as *microscopic c.m. correction* throughout this paper, referring to the fact that it is calculated from the actual many–body state. The explicit dependence on mass number of (1) might cause some trouble when calculating mass differences, see [12]. In the framework of energy density functionals, the factor A should be replaced by the integral of the local isoscalar density; since we will use (1) for correction–after–variation only throughout this paper, however, this would make no difference.

$\hat{\mathbf{P}}_{\mathrm{cm}} = \sum_{\mathrm{k}} \hat{\mathbf{p}}_{\mathrm{k}}$ is the total momentum operator in the center–of–mass frame, which is given by the sum of the single–particle momentum operators. Although the BCS state has vanishing total momentum $\langle\hat{\mathbf{P}}_{\mathrm{cm}}\rangle = 0$, it is not an eigenstate of $\hat{\mathbf{P}}_{\mathrm{cm}}$, but has a non–vanishing expectation value of its square

$$\langle\hat{\mathbf{P}}^2_{\mathrm{c.m.}}\rangle = \sum_{\alpha} \mathrm{v}^2_\alpha\ \mathrm{p}^2_{\alpha\alpha} - \sum_{\alpha,\beta} \mathrm{v}^2_\alpha \mathrm{v}^2_\beta\ \mathbf{p}_{\alpha\beta}\cdot\mathbf{p}^*_{\alpha\beta} + \sum_{\alpha,\beta} \mathrm{v}_\alpha \mathrm{u}_\alpha \mathrm{v}_\beta \mathrm{u}_\beta\ \mathbf{p}_{\alpha\beta}\cdot\mathbf{p}_{\bar{\alpha}\bar{\beta}} \quad . \tag{2}$$

The α and β denote single-particle states. The $\mathrm{p}^2_{\alpha\alpha}$ are single–particle expectation values of the square of the single–particle momentum operator. They appear only in the direct term of the correction. The $\mathbf{p}_{\alpha\beta}$ are off-diagonal single–particle matrix elements of the momentum operator. Their squares result from the exchange terms in $\langle\hat{\mathbf{P}}^2_{\mathrm{cm}}\rangle$. The further evaluation of (2) is outlined in the Appendix.

Although $\mathrm{E^{mic}_{c.m.}}$ as given by (1) is already the first–order approximation for the momentum–projected binding energy there exist numerous further approximations for $\mathrm{E^{mic}_{c.m.}}$ in the literature:

(A) The full correction (2) is considered in the variational equation and the calculation of the binding energy $\mathrm{E_{tot}}$

$$\delta(\mathcal{E}_{\mathrm{int}} - \mathrm{E^{mic}_{c.m.}}) = 0 \quad , \quad \mathrm{E_{tot}} = \mathcal{E}_{\mathrm{int}} - \mathrm{E^{mic}_{c.m.}} \quad . \tag{3}$$

This was employed so far only in the fit of the Skyrme interactions SLy6 and SLy7 [13,14]. For HF states without pairing $\mathrm{E_{c.m.}}$ gives an additional term to the equations–of–motion but the HF equations can be solved as usual. For HFB states the mean field becomes state dependent, which requires an additional constraint on orthonormal single–particle wave functions in the variational equation as described in [15]. The numerical solution of the resulting equations of motion is very costly, especially in deformed calculations. Therefore this scheme was employed so far only for the description of doubly–magic nuclei where an HF state can be used.

(B) The c.m. correction is omitted in the variational equations, but the microscopic correction (2) is considered when calculating the total binding energy

$$\delta\mathcal{E}_{\mathrm{int}} = 0 \quad , \quad \mathrm{E_{tot}} = \mathcal{E}_{\mathrm{int}} - \mathrm{E^{mic}_{c.m.}} \quad . \tag{4}$$

This *a posteriori* correction scheme is used, e.g., for the Skyrme forces SkI1–SkI5 [16] and the RMF forces NL–Z [17], and PL–40 [19].

Table 1. Compilation of nuclear matter properties for a number of typical parameter sets. SkM*–SLy6 are Skyrme forces, D1 and D1S are Gogny interactions, and NL1, NL–Z, NL3, and NL–SH RMF forces. 'scheme' is the scheme for c.m. correction employed in the fit of the particular interaction, a_{vol} denotes the volume coefficient or energy per nucleon, a_{sym} the (volume) symmetry coefficient, and a_{surf} the surface coefficient. Empirical values for the volume coefficients derived from the liquid–drop model are $a_{vol} = -16.0 \pm 0.2$ and $a_{sym} = 32.5 \pm 0.5$ [41].

Force	Ref.	scheme	a_{vol} [MeV]	a_{sym} [MeV]	a_{surf} [MeV]
SkM*	[21]	C	−15.75	30.0	17.6
SkP	[22]	C	−15.92	30.0	18.0
SkT6	[23]	C	−15.94	30.0	18.1
E_σ	[5]	C	−16.00	26.5	18.2
Z_σ	[5]	B	−15.85	26.7	16.9
SkI1	[16]	B	−15.93	37.5	17.3
SkI3	[16]	B	−15.96	34.8	17.5
SkI4	[16]	B	−15.92	29.5	17.3
SLy4	[14]	C	−15.97	32.0	18.2
SLy6	[14]	A	−15.92	32.0	17.4
D1	[25]	C	−16.02		20.3
D1S	[26]	C	−16.02		18.2
NL1	[30]	E	−16.42	43.5	18.7
NL-Z	[17]	B	−16.19	41.7	17.7
NL3	[29]	D	−16.24	37.4	18.5
NL-SH	[27]	D	−16.35	36.1	19.1

(C) The c.m. correction is approximated by its diagonal (direct) terms

$$E^{dir}_{c.m.} = \frac{1}{2mA} \sum_k v_k^2 \, p_{kk}^2 = -\frac{\hbar^2}{2mA} \int dr \, \tau \qquad (5)$$

– where τ is the local kinetic density – but employed before variation

$$\delta(\mathcal{E}_{int} - E^{dir}_{c.m.}) = 0 \quad , \quad E_{tot} = \mathcal{E}_{int} - E^{dir}_{c.m.} \quad . \qquad (6)$$

The contribution from the c.m. correction to the (non–relativistic) equations of motion has the same structure as the kinetic term and leads to a renormalisation of the mass of the nucleons

$$\frac{1}{m} \to \frac{1}{m}\left(1 - \frac{1}{A}\right) \quad . \qquad (7)$$

This scheme is used for most Skyrme interactions like SIII [20], SkM* [21], SkP [22], the Skyrme forces of Tondeur [23], SLy4 and SLy5 [14], the Skyrme interactions used in semi–microscopic ETFSI calculations [24], and the Gogny forces [25].

(D) The microscopic c.m. correction (1) can be evaluated analytically for harmonic oscillator states. Using the usual parameterisation of the oscillator constant from the Nilsson model one obtains an estimate for (1) as

$$E^{osc}_{c.m.} = -\tfrac{3}{4} \, 41 \, A^{-1/3} \text{ MeV} \quad . \qquad (8)$$

This is used for the RMF forces NL–SH [27], TM1 [28], and NL3 [29]. Because (8) does not depend on the many–body wave function this gives no contribution to the variational equations.

(E) The c.m. correction is approximated by

$$E^{fit}_{c.m.} \approx -17.2 \, A^{-0.2} \text{ MeV} \qquad (9)$$

which is a fit to values of the full *a posteriori* correction for the fit nuclei calculated with the Skyrme interaction Z_σ [5]. This is used for the RMF forces NL1 and NL2 [30].

Some of these approximate schemes for c.m. correction are discussed and compared in [31], where also an additional one is proposed which is not used in the models discussed here and a short historical overview is given. However, the authors of [31] restrict themselves to the quality of the various schemes to approximate (1).

As can be seen from the harmonic oscillator value (8) – which will turn out to give at least the right order of magnitude for $E^{mic}_{c.m.}$ in heavy nuclei – the c.m. correction decreases with increasing mass number A and vanishes for infinite homogeneous nuclear matter (which is translationally invariant). Since the total binding energy increases with A, the relative contribution of the c.m. correction to the total binding energy is largest for very small nuclei.

In the correction–before–variation schemes (A) and (C) the c.m. correction directly affects other observables than the total binding energy as well, for example single–particle energies. Like in case of the total binding energy the effect of the correction decreases with increasing A. All other schemes deliver an approximate correction of the binding energy only, but analogous a posteriori correction of order $\langle \hat{\mathbf{P}}_{c.m.} \rangle$ can be performed for the local density $\rho(\mathbf{r})$ and with that all observables derived from it [7,32].

We mention in passing that no c.m. correction of the binding energies is performed in macroscopic–microscopic models, but the smooth part of $E_{c.m.}$ is implicitly contained in the macroscopic part of these models.

4 Results and Discussion

4.1 Nuclear Matter Properties

From the model systems of infinite nuclear matter (INM) and semi-infinite nuclear matter (SINM) at saturation density one obtains the leading terms in the nuclear liquid-drop mass formula

$$E = a_{vol} \, A + a_{sym} \, I^2 \, A + a_{surf} \, A^{2/3} + \ldots \quad , \qquad (10)$$

where A is the mass number and I the relative neutron excess given by $I = (N - Z)/A$. The relation between self–consistent mean–field models and the liquid–drop model and its refinements like the droplet model is discussed in [39]. While the volume coefficient a_{vol} and volume symmetry coefficient a_{sym} calculated in INM are directly comparable with the liquid–drop values, the surface coefficient

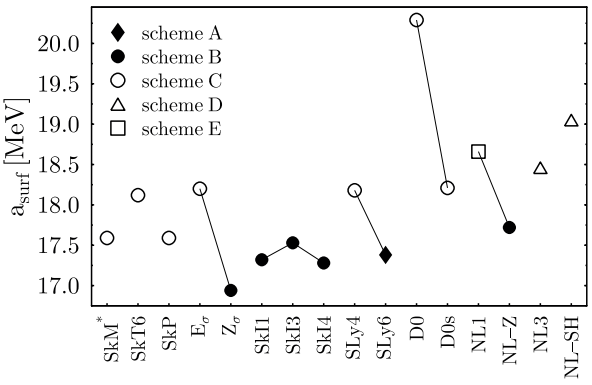

Fig. 1. Surface coefficient a_{surf} for a variety of effective interactions. Lines connect interactions which are similarly fitted. Open markers denote forces with a simple scheme for c.m. correction, while filled markers denote interactions where $E_{c.m.}$ is calculated microscopically within scheme (A) or (B). The interactions with microscopically calculated $E_{c.m.}$ have significantly smaller surface coefficients.

a_{surf} has to be handled more carefully. Usually a_{surf} is extracted from calculations of SINM in semi–classical approximation which leads to a value of the surface coefficient that is not directly comparable to the liquid–drop model value [39,42,43]. Instead the particular Skyrme interaction SkM* – which is fitted with emphasis on its surface properties – is often used as a reference when discussing the surface coefficient of effective interactions.

The INM properties of effective interactions have been extensively discussed elsewhere, see e.g. [7,18,39–41] and references therein. The properties of SINM have gained a lot of attention as well, see e.g. [21,23,39,42–46] for non–relativistic models and [47–54] for relativistic interactions. We just want to repeat the findings relevant for our study, Table 1 summarises the coefficients of (10) as calculated from symmetric INM and SINM for a number of effective interactions. Most non–relativistic (relativistic) interactions agree among each other in the values for a_{vol} and a_{sym} although there are some minor differences and a few exceptions, but relativistic and non–relativistic interactions differ significantly, the RMF forces give a_{vol} and a_{sym} larger than the empirical values, while the Skyrme forces work much better in that respect. It is important to note, however, that not all the values for Skyrme forces are predictions. For some parametrisations, i.e. SLy4, SLy6, SkP, SkT6 and SkM*, INM properties were used as input data during their fit.

The values for the surface coefficient a_{surf} differ significantly among all effective interactions, see also Fig. 1. We present here values calculated with the extended Thomas–Fermi method taken from [53] or calculated with the code of M. Brack [55]. The interactions using $E^{mic}_{c.m.}$ have systematically smaller surface coefficients a_{surf} than most of the other interactions. This hints at a correlation between the scheme for c.m. correction and the surface tension of an effective interaction, which becomes obvious when looking at pairs of effective forces which are fitted in exactly the same way but use different schemes for the c.m. correction: the non–relativistic E_σ and Z_σ, SLy4 and SLy6 and the relativistic NL1 and NL–Z. In all cases the interaction employing $E^{mic}_{c.m.}$ has a value of a_{surf} smaller by roughly 1.0 MeV compared to the interaction employing a simpler scheme for the c.m. correction.

Although the Skyrme force SkM* employs the simple scheme (C) for the c.m. correction, it gives also a rather low value for a_{surf}. As already mentioned, SkM* is an exception among the interactions discussed here because it was aimed at giving better a_{surf} via fitting the fission barrier of ^{240}Pu after it was found that all earlier Skyrme interactions give wrong values for the surface coefficient [21,39]. SkM* still serves as a reference for the surface properties of effective interactions for self–consistent models. Similar emphasis on proper INM and SINM properties was taken for SkP [22], again resulting in a low value for a_{surf}. All Skyrme interactions employing $E^{mic}_{c.m.}$ for the c.m. correction, however, give a similar (small) value for a_{surf} as SkM* which leads to the conclusion that effective interactions using the microscopic c.m. correction give a reasonable value for a_{surf} *without* taking explicit information on the surface coefficient into account when fitting them while interactions with simpler c.m. correction need additional information on the surface tension to give proper surface properties.

This is confirmed when looking at another pair of similarly fitted interactions: the Gogny forces D1 and D1S. Both are fitted with the diagonal approximation $E^{dir}_{c.m.}$ for c.m. correction, scheme (C), but D1S is a refit of the original interaction taking again explicit information on the deformation energy of heavy nuclei into account [26].

In the remaining part of the paper we want to investigate the reason for that correlation and give some typical examples for the influence of the difference in the c.m. correction and the surface coefficient on observables. To that end, we have chosen from all parametrisations discussed above a pair of Skyrme interactions, i.e. SLy4 and SLy6, and a pair of RMF forces, i.e. NL1 and NL–Z, which are fitted in the same way but use different levels of approximation for the c.m. correction. The first pair compares scheme (C) with scheme (B) while the second pair compares schemes (E) and (B). As already mentioned, the correction before variation used for SLy6 becomes very complicated in connection with BCS states. Therefore we follow the suggestion of [14] and use the *a posteriori* microscopic correction scheme (B) instead which was already done in [34,35].

4.2 Binding energy of spherical nuclei

The fit of effective interactions for self–consistent nuclear structure models is usually performed with spherical doubly–magic or semi–magic nuclei. The origin of the correlation between surface tension and the scheme for c.m. correction found above can be understood looking at the systematics of the c.m. correction throughout the chart of nuclei, see Fig. 2, which shows $E_{c.m.}$ drawn versus the mass

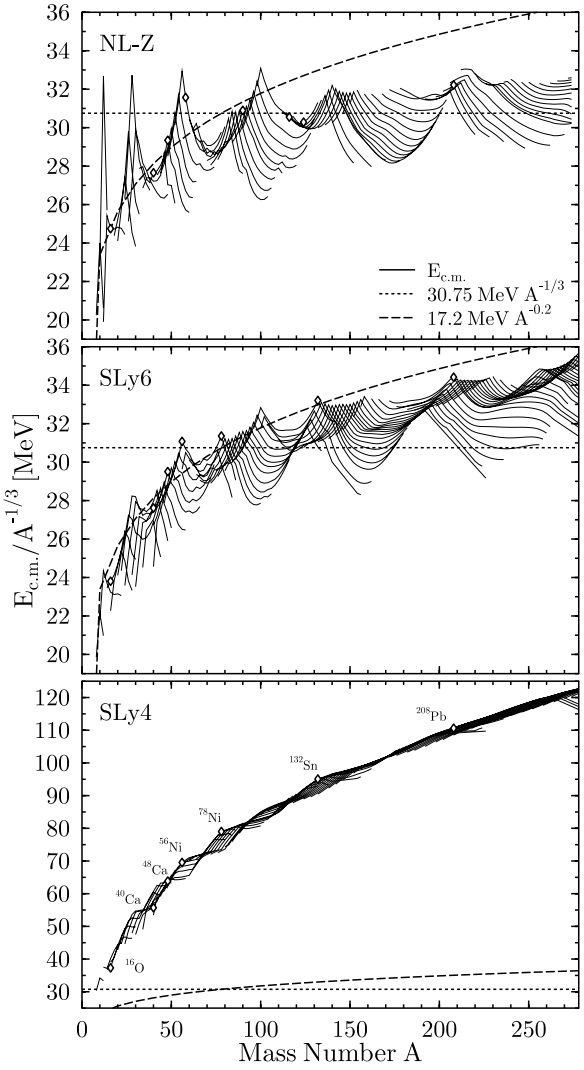

Fig. 2. Amplitude of the correction for center–of–mass motion $E_{c.m.}$ in spherical calculations with the RMF force NL–Z (upper panel), and the Skyrme interactions SLy6 (middle panel) and SLy4 (lower panel). The results are scaled with $A^{-1/3}$ to remove the smooth trend of the microscopic c.m. correction with A. Solid lines connect nuclei in isotopic chains, the dashed line is the fit (9) used for NL1, the dotted line the harmonic oscillator estimate (8). The diamonds denote the nuclei used in the fit of the particular interaction

number A calculated in spherical symmetry for even–even nuclei between the (calculated) two–nucleon drip–lines.

Looking at the results for NL–Z, one sees that the c.m. correction shows pronounced shell effects and has maximum values at shell closures. $E^{mic}_{c.m.}$ is a measure for the localisation of the many–body wave function and in magic nuclei the density distribution is indeed somewhat more localised: rms-radii and surface thicknesses are smaller than the value obtained from interpolating between adjacent nuclei, which in turn leads to a larger value for the variance of the total momentum $\langle \hat{\mathbf{P}}^2_{c.m.} \rangle$. It is to be noted that the results from calculations in spherical symmetry plotted in Fig. 2 may not be taken too seriously when one is far away from proton and neutron shell closures: there the nuclei can be expected to be deformed with a more localised density distribution and somewhat larger $E_{c.m.}$. However, this does not affect the conclusions drawn here.

For heavy nuclei A > 100 $E^{mic}_{c.m.}$ oscillates around $E^{osc}_{c.m.}$, while $E^{fit}_{c.m.}$ gives a better approximation to $E^{mic}_{c.m.}$ for small nuclei up to ^{90}Zr, but overestimates $E^{mic}_{c.m.}$ of heavy nuclei. It is noteworthy that none of the algebraic schemes for the c.m. correction used so far is able to approximate the smooth trend of $E^{mic}_{c.m.}$ reasonably for all nuclei throughout the chart of nuclei. Improved fits are of course possible, but the shell effects visible in Fig. 2 can be described only when $E^{mic}_{c.m.}$ is employed for the c.m. correction.

At a first glance the results for SLy6 look very similar to those obtained with NL–Z, but there are some significant differences: The shell oscillations of $E^{mic}_{c.m.}$ for small nuclei are much smaller in the SHF than in the RMF and $E^{mic}_{c.m.}$ from SLy6 decreases more slowly with increasing mass number than $E^{mic}_{c.m.}$ from NL–Z. This explains why $E^{fit}_{c.m.}$ used for the RMF force NL1 is so far off $E^{mic}_{c.m.}$ for NL–Z: The fit (9) was performed using values of $E^{mic}_{c.m.}$ calculated with the Skyrme interaction Z_σ which gives results very similar to those for SLy6 but which are again too large compared to values calculated from RMF model wave functions.

The results for $E^{dir}_{c.m.}$ used for SLy4 are qualitatively and quantitatively very different compared to $E^{mic}_{c.m.}$ used with NL–Z and SLy6: the shell fluctuations have nearly vanished and – even more important – the diagonal part $E^{dir}_{c.m.}$ does not scale with $A^{-1/3}$. This demonstrates that the exchange contributions to $E^{mic}_{c.m.}$ are of the same order as the direct terms – but with opposite sign – and cancel them nearly which gives the A dependence of $E^{mic}_{c.m.}$ found for NL–Z and SLy6.

The wrong trend of $E^{dir}_{c.m.}$ (as compared to $E^{mic}_{c.m.}$) with A has to be compensated by the effective interaction $\mathcal{E}_{int}$ in order to obtain the proper binding energy of the (fit) nuclei. This is the key to understand the large differences in the surface tension found in Sect. 4.1: The error in the A dependence of simple schemes for c.m. correction puts a wrong A dependence into the effective interaction which reveals itself in the nuclear matter properties.

It is instructive to fit the difference $\Delta E_{c.m.} = E^{dir}_{c.m.} - E^{mic}_{c.m.}$ between the two schemes for c.m. correction for the nuclei used in the fit of the interactions SkM*, E_σ, and SLy4, with the simple mass formula

$$\Delta E_{c.m.} = \tilde{a}_{vol}\, A + \tilde{a}_{surf}\, A^{2/3} \quad . \tag{11}$$

The resulting values for the parameters $\tilde{a}_{vol}$ and $\tilde{a}_{surf}$ are given in Table 2 together with the actual differences Δa_{vol} and Δa_{surf} between the nuclear matter properties of pairs the similar fitted interactions E_σ and Z_σ, respectively SLy4 and SLy6. First of all it is remarkable that the coefficients $\tilde{a}_{vol}$ and $\tilde{a}_{surf}$ are very similar for all interactions, which means that the amplitude of the c.m. correction is very similar for all non–relativistic interactions. In the ideal case the nuclear matter properties of an effective interaction fitted with a simple c.m. correction

Table 2. Coefficients $\tilde{a}_{vol}$ and $\tilde{a}_{surf}$ of the liquid–drop expansion (11) of the difference between $E^{mic}_{c.m.}$ and $E^{dir}_{c.m.}$ calculated for the fit nuclei of some Skyrme forces which use the diagonal approximation scheme (C). For those parameterisations where an equally fitted interaction with full microscopic c.m. correction exists, Δa_{vol} (Δa_{surf}) gives the difference between the volume (surface) coefficients of those interactions, e.g. $\Delta a_{surf}(SLy4) = a_{surf}(SLy4) - a_{surf}(SLy6)$. Most of the Skyrme interactions using scheme (C) which are listed in Table 1 are mainly fitted to nuclear matter properties (and to a few finite nuclei only) and therefore omitted

Force	$\tilde{a}_{vol}$ [MeV]	$\tilde{a}_{surf}$ [MeV]		Δa_{vol} [MeV]	Δa_{surf} [MeV]
SkM*	−0.14	1.2	–	–	–
E_σ	−0.13	1.2	$E_\sigma - Z_\sigma$	−0.15	1.3
SLy4	−0.15	1.2	SLy4−SLy6	−0.05	0.8

would be larger by the values of the coefficients of (11) than the nuclear matter properties of a force fitted in the same way but using $E^{mic}_{c.m.}$. This is indeed the case for E_σ and Z_σ where $\tilde{a}_{vol} \approx \Delta a_{vol}$ and $\tilde{a}_{surf} \approx \Delta a_{surf}$. However, for other interactions things are complicated by the fact that several nuclear matter properties were constrained during the fit, hiding (but not curing) the problems caused by the simple schemes for c.m. correction. The constraint on a_{vol} for SLy4 and SLy6 diminishes the difference Δa_{vol} and probably with that also the difference Δa_{surf} but one can expect that there are instead larger differences than necessary in the higher–order terms of the liquid–drop expansion since $\Delta E_{c.m.}$ itself is not affected by constraints on nuclear matter properties. Including symmetry terms in (11) neither improves the quality of the fit nor significantly changes the values of $\tilde{a}_{vol}$ and $\tilde{a}_{surf}$. This simple picture works well to explain how the use of the approximate c.m. correction scheme (C) affects nuclear matter properties of non–relativistic interactions. The fits of $\Delta E_{c.m.}$ with (11) for these interactions give an average deviation of $\delta\Delta E^2_{c.m.} \approx 0.09\,\mathrm{MeV}^2$.

For the RMF, however, the usual approximations are schemes (D) and (E). Here, the mass formula (11) gives very bad fits of $\Delta E_{c.m.}$ with $\delta\Delta E^2_{c.m.} \approx 0.6\,\mathrm{MeV}^2$ for all interactions. To obtain a fit of the same quality as in the case of non–relativistic interactions a curvature term has to be included

$$\Delta E_{c.m.} = \tilde{a}_{vol}\,A + \tilde{a}_{surf}\,A^{2/3} + \tilde{a}_{curv}\,A^{1/3} \quad , \qquad (12)$$

which yields again an acceptable error of $\delta\Delta E^2_{c.m.} \approx 0.09\,\mathrm{MeV}^2$. The actual values of the coefficients $\tilde{a}_i$ are listed in Table 3. The volume and surface coefficients are of similar size as in case of the SHF model. In the RMF we have a pair of similarly fitted forces, namely NL1 with the recipe (E) and NL–Z with the microscopic c.m. correction (B). And again, the differences of nuclear matter properties between these forces are quite close to the coefficients $\tilde{a}_i$ for NL1: $\tilde{a}_{vol} \approx \Delta a_{vol} = -0.23$ MeV and

Table 3. Coefficients of the liquid–drop expansion (12) of the difference between $E^{mic}_{c.m.}$ and the approximation to it used for some relativistic forces. To obtain a fit of the same quality as in case of the Skyrme forces discussed above a curvature term has to be included.

Force	$\tilde{a}_{vol}$ [MeV]	$\tilde{a}_{surf}$ [MeV]	$\tilde{a}_{curv}$ [MeV]
NL1	−0.12	1.2	−3.2
NL3	−0.11	1.1	−2.7
NL–SH	−0.10	1.0	−2.4

$\tilde{a}_{surf} \approx \Delta a_{surf} = 1.0$ MeV. Altogether we find that the RMF behaves much similar as the SHF concerning the impact of the c.m. correction on extrapolation to nuclear matter properties.

One may have the impression that the correlation between the recipe for the c.m. correction and the emerging surface tension is a merely technical problem, but one has to be aware that the choice of the recipe has remarkable consequences for extrapolations. Besides the different extrapolation of total binding energies visible in Fig. 2, we discuss in what follows the dramatic consequences for strongly deformed systems.

4.3 Deformation Energy of Heavy Nuclei

We have already seen that a different treatment of the c.m. correction in the fit of an effective interaction leads to very different surface properties even when the interactions are otherwise fitted in exactly the same way. To get an impression of the amplitude of this effect, we now look at superdeformed states and fission barriers of heavy nuclei, where experimental information about the deformation energy is available even for very large deformations. As an example we have chosen ^{240}Pu which provides the standard testing ground for the capability of self-consistent nuclear mean–field models to describe fission barriers, see e.g. [21,26,56–59].

In the following we will present deformation energy curves calculated in axial symmetry, allowing for reflection asymmetric shapes with a damped quadrupole constraint; for numerical details see [59]. The deformation energy curves are shown versus the dimensionless quadrupole moment of the mass density which is defined as

$$\beta_2 = \frac{4\pi}{3Ar_0^2}\,\langle r^2\,Y_{20}\rangle \quad \text{with } r_0 = 1.2\,A^{1/3}\ \mathrm{fm}$$

and which has to be distinguished from the generating deformation parameter which is used in macroscopic–microscopic models [33].

The upper panel of Fig. 3 shows the deformation energy of ^{240}Pu calculated in the SHF model with the interactions SLy4 and SLy6. The first barrier is slightly lowered for triaxial shapes which are not considered here, but this

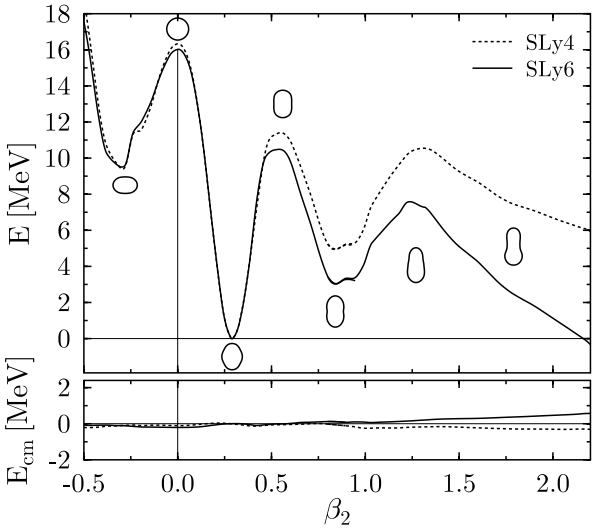

Fig. 3. Deformation energy (normalised to the prolate ground state) of ^{240}Pu calculated with the Skyrme interactions SLy4 and SLy6. The lower panel shows the change of the c.m. correction compared to the ground–state value in the same scale as the deformation energy in the upper panel. The various shapes along the fission path are indicated by the contours of the density at $\rho_0 = 0.07\,\mathrm{fm}^{-3}$.

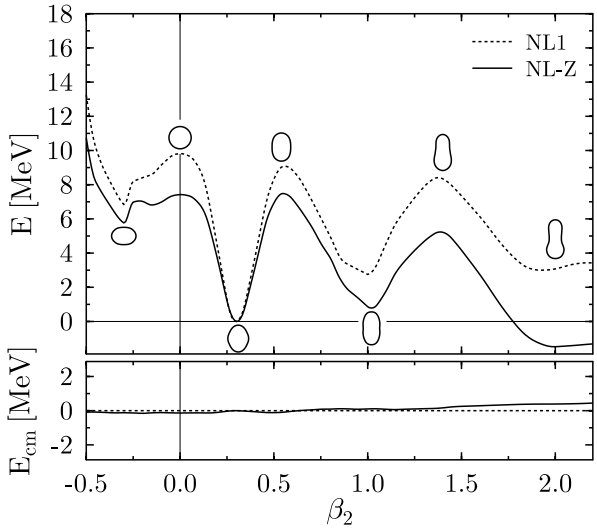

Fig. 4. Fission barrier of ^{240}Pu calculated with the RMF forces NL1 and NL–Z drawn in the same manner and using the same scales as in Fig. 3.

has no influence on the conclusions drawn in this paper. The authors of [35], however, report a reduction of the first barrier of 2.1 MeV for SLy4 when allowing for triaxial shapes. For deformations smaller than the value at the isomeric state at $\beta_2 = 0.85$, the minimum configurations turn out to be reflection symmetric, while for larger deformations the fission path prefers asymmetric shapes.

Both Skyrme interactions give very similar deformation energy at small deformations inside the first barrier, but beyond the first barrier a significant difference between the deformation energy curves of SLy4 and SLy6 becomes visible which increases steadily with deformation. At the second, superdeformed (SD) minimum the difference is already 1.9 MeV and increases to 6.3 MeV at $\beta_2 = 2.2$. SLy4 gives a much broader and higher fission barrier than SLy6 which will make a huge difference when calculating fission half-lives. The difference between the interactions is not caused by the variation of the c.m. correction with deformation as can be seen in the lower panel of Fig. 3; it is caused by the difference in a_{surf} between the two interactions. This was already noticed by the authors of [14].

The excitation energy of the SD minimum is determined mainly by the interplay of two very different effects: The variation of surface (and surface symmetry) energy with deformation contained in the bulk properties of the effective interaction (the Coulomb energy which varies with deformation as well is nearly the same for all interactions) and the variation of shell effects with deformation (which is fixed by the shell structure at spherical shape). SLy4 and SLy6 give nearly the same single–particle energies for spherical nuclei, the fission paths are identical, the difference visible in Fig. 3 is caused only by the difference in surface tension between the two interactions.

This gives a possible explanation for the finding of the authors of [35] that the Skyrme interaction SLy4 overestimates the excitation energy of the SD minima in nuclei around $A \approx 190$ and $A \approx 240$ while it reproduces nicely the separation energies within the first and SD minima. In each region either all ground–states and all SD minima have roughly the same deformation, therefore the separation energy calculated between states in the same well is not affected by the surface tension. This might explain also to some extent the preference for SkM*, SkI3 and SkP for the description of superdeformed states in ^{194}Hg found in [37]. All three forces have rather small surface coefficients a_{surf} (see Table 1 and Fig. 1), SkI3 because it employs the microscopic c.m. correction, SkM* and SkP because the value of a_{surf} was constrained during the fit of these particular interactions. However, the excitation energy of superdeformed states is determined by the interplay of surface properties and shell structure, both have to be properly described to reproduce experimental data throughout the whole chart of nuclei. More investigation in that direction is needed.

Figure 4 shows the same as Fig. 3, but for the RMF forces NL1 and NL–Z. The qualitative features of the fission barrier are the same as those found for the Skyrme forces, but there are significant quantitative differences. Comparing both figures it can be clearly seen that all barriers are much smaller for the RMF forces compared to the Skyrme interactions. Again, the RMF force which employs the "cheaper" c.m. correction gives the larger deformation energy compared to the ground-state value. There are now some differences between NL1 and NL–Z at small deformations as well, but for large prolate deformations we regain our finding for the Skyrme forces: The difference in the deformation energy increases with deformation, it is al-

ready 1.9 MeV at the SD minimum and 4.7 MeV around $\beta_2 = 2.2$. The RMF forces shift the SD minimum to a slightly larger deformation $\beta_2 \approx 1.0$ than the SLyx forces. For NL–Z the excitation energy of the SD minimum of −0.8 MeV is definitively too small compared to the experimental value of 2.4 MeV, while the value of 2.8 MeV predicted by NL1 is quite close. We expect, however, that the better description of the SD state obtained with NL1 is accidental because the surface coefficient of this interaction is definitively too large.

Again the difference of the deformation energy curves is not caused by the actual contribution of the c.m. correction to the binding energy, see the lower panel of Fig. 4. $E_{c.m.}^{mic}$ varies only by a few 100 keV along the fission path while the value for $E_{c.m.}^{fit}$ is of course constant.

We have to revise our conclusions from [59] where the fission barriers of ^{240}Pu calculated with PL–40 [19] and NL1 were compared. Both interactions are fitted in the same way but differ in two details: the treatment of the c.m. correction – where PL–40 employs the same scheme as NL–Z – and the density dependence, where NL1 and NL–Z employ the standard non–linear self-interaction of the scalar field while PL–40 uses a stabilised self-interaction, see [7,19] for details. We have concluded in [59] that the difference between the fission barriers is caused by the difference in the density dependence of the two forces PL–40 and NL1, but as can be seen comparing Fig 4 with the results of [59] NL–Z and PL–40 give very similar fission barriers, therefore the difference between NL1 and PL–40 is caused by the different treatment of the c.m. correction during the fit of these interactions. This means in turn that using the stabilised non–linearity instead of the standard non–linearity in the RMF has only a very small influence on the fission barriers of heavy nuclei.

It is to be noted that the mere c.m. correction (1) becomes inconsistent in the asymptotics of fission (i.e. beyond the scission point). One still would use one common $E_{c.m.}$ whereas the two fragments should now acquire each their own $E_{c.m.}$. The problem can be resolved by including also the correction for spurious quadrupole vibrations [60, 61]. But this complication can be neglected when looking at the fission barrier of heavy nuclei where the scission point is far beyond the fission point.

4.4 Deformation Energy of Light Nuclei

Figure 5 shows the deformation energy for the nucleus ^{44}S calculated again with SLy4, SLy6, NL1, and NL–Z. The potential landscapes for the relativistic and non–relativistic interactions look very different: SLy4 and SLy6 predict a rather soft potential energy surface with a shallow oblate minimum, while NL1 and NL–Z predict an energy surface with deep prolate and oblate minima of comparable binding energy (which might be connected by triaxial configurations). The main difference between the models appears at small deformations around $\beta_2 = 0$, while all interactions give similar predictions for the deformation of the prolate and oblate minima respectively. This

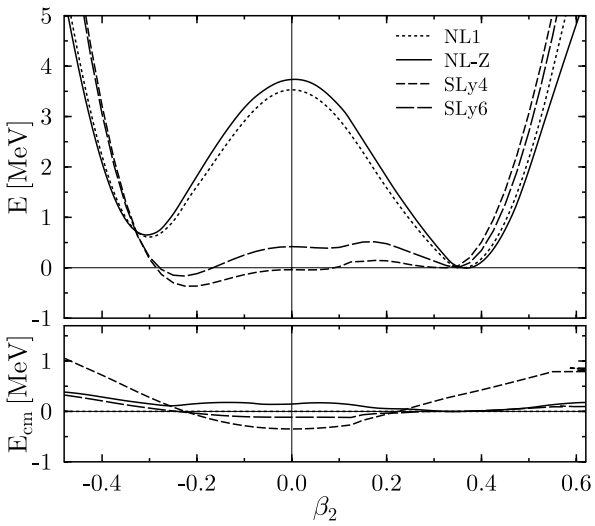

Fig. 5. Deformation energy (upper panel) and variation of the c.m. correction (lower panel) of ^{44}S calculated with NL1, NL–Z, SLy4 and SLy6. The deformation energy E and the c.m. correction $E_{c.m.}$ are normalised to their values at the prolate minimum. The two panels use again the same energy scale.

is interesting for itself as it has dramatic influence on the excitation spectrum of this nucleus, but we do not want to discuss this further here and refer to [38] and references therein.

In contrast to the heavy system ^{240}Pu there now appear visible differences at small deformations as well, which are directly related to the different variation of $E_{c.m.}^{dir}$ and $E_{c.m.}^{mic}$ with deformation, see the lower panel of Fig. 5. Comparing SLy4 and SLy6, one sees that the diagonal part of the c.m. correction oscillates with larger amplitude than the full correction including exchange terms. The relativistic forces NL1 and NL–Z show a small difference at small deformations as well, but this difference has another origin: $E_{c.m.}^{mic}$ is slowly varying while the fit value is simply constant. At large prolate deformations the difference in surface tension between SLy4 and SLy6 gives again a large difference between the potential energy surfaces. The differences caused by the c.m. correction among these particular relativistic and non–relativistic forces are rather small compared to the difference between the predictions of the non–relativistic and relativistic models and it is to be noted that SLy4 and SLy6 are by no means representative for the predictions of Skyrme interactions, see [38]. However, the differences we see for small nuclei at small deformations caused by differences in the variation of the c.m. correction with deformation are subtle compared to the huge effect caused by the difference in surface tension seen at large deformations.

5 Summary

We have discussed the various approximate schemes for performing the c.m. correction in connection with self–

consistent mean–field models. In particular, we have scrutinised the effect of the actual recipe for the c.m. correction used while fitting a parametrisation. The basic point is that the different recipes differ in their trends with mass number A and isospin. Mismatches thus inherent in a recipe are counterweighted to a certain extend by (automatic) readjustments of the model parameters. This, in turn, builds into the forces different properties concerning extrapolations.

We have considered the c.m. correction of order $\langle\hat{\mathbf{P}}^2_{\mathrm{c.m.}}\rangle$ throughout. The full evaluation of $\mathrm{E}^{\mathrm{mic}}_{\mathrm{c.m.}}$ was compared with the approximation through the diagonal part of that expression and with a simple estimate $\propto \mathrm{A}^{-\gamma}$. The comparison of the c.m. correction as such shows significant differences between these three schemes. The full correction shows considerable shell effects which are completely absent in all simple estimates. Moreover, the average trends of $\mathrm{E}_{\mathrm{c.m.}}$ with A and I of these three recipes differ, which has consequences for the properties of effective interactions fitted with simple schemes for c.m. correction. We see a strong effect on the surface energy where the forces with approximate c.m. correction (diagonal part or simple estimate) give systematically larger values than interactions employing $\mathrm{E}^{\mathrm{mic}}_{\mathrm{c.m.}}$.

This error in surface energy leads to a much different evolution of energies with deformation. As a consequence, fission barriers in actinide nuclei are about 4 MeV larger for those forces which employed the approximate recipes during their fit. Furthermore, predictions of the relative height of deformation isomers and collective vibrations therein will come out significantly different. For light nuclei – where the relative importance of the c.m. correction is larger – one even has to be aware of differences at small deformations. Altogether, we strongly recommend to use consistently the full correction $\langle\hat{\mathbf{P}}^2_{\mathrm{c.m.}}\rangle/(2\mathrm{mA})$ and forces derived with that recipe. Any further approximation beyond that (already approximate) stage induces systematic errors in extrapolation to heavy nuclei, large deformation, and probably also to nuclei far off the stability line.

The authors thank W. Nazarewicz for useful comments. This work was supported by Bundesministerium für Bildung und Forschung (BMBF), Project No. 06 ER 808 and by the U.S. Department of Energy under Contract No. DE–FG02–96ER40963 with the University of Tennessee and Contract No. DE–FG02–97ER41019 with the University of North Carolina and by the NATO grant SA.5–2–05 (CRG.971541). The Joint Institute for Heavy Ion Research has as member institutions the University of Tennessee, Vanderbilt University, and the Oak Ridge National Laboratory; it is supported by the members and by the Department of Energy through contract No. DE–FG05–87ER40361 with the University of Tennessee.

A The Calculation of $\langle\hat{\mathbf{P}}^2_{\mathrm{c.m.}}\rangle$

In this appendix we present the formulae needed to calculate the expectation value of $\langle\hat{\mathbf{P}}^2_{\mathrm{c.m.}}\rangle$ in relativistic and non–relativistic models assuming spherical, axial symmetry or triaxial symmetry for a BCS many–body state. Expressing (2) in terms of matrix elements $\Delta_{\alpha\alpha}$ of the Laplacian and $\nabla_{\alpha\beta}$ of the nabla operator respectively, one obtains

$$\begin{aligned}\langle\hat{\mathbf{P}}^2_{\mathrm{c.m.}}\rangle &= -\hbar^2\Big[\sum_{\alpha\gtrless 0}\mathrm{v}^2_\alpha\,\Delta_{\alpha\alpha}+\sum_{\alpha,\beta\gtrless 0}\big(\mathrm{v}^2_\alpha\,\mathrm{v}^2_\beta\,\nabla_{\alpha\beta}\cdot\nabla^*_{\alpha\beta}\\ &\quad -\mathrm{v}_\alpha\mathrm{u}_\alpha\mathrm{v}_\beta\mathrm{u}_\beta\,\nabla_{\alpha\beta}\cdot\nabla_{\bar\alpha\bar\beta}\big)\Big]\quad . \end{aligned}\tag{13}$$

In case of a time–even many–body state this simplifies with $\Delta_{\bar\alpha\bar\alpha}=\Delta_{\alpha\alpha}$, $\nabla_{\bar\alpha\bar\beta}=\nabla^*_{\alpha\beta}$ and $\nabla_{\bar\alpha\beta}=-\nabla^*_{\alpha\bar\beta}$ to

$$\begin{aligned}\langle\hat{\mathbf{P}}^2_{\mathrm{c.m.}}\rangle &= -2\hbar^2\Big[\sum_{\alpha>0}\mathrm{v}^2_\alpha\,\Delta_{\alpha\alpha}+\sum_{\alpha,\beta>0}\mathrm{v}_\alpha\mathrm{v}_\beta(\mathrm{v}_\alpha\mathrm{v}_\beta+\mathrm{u}_\alpha\mathrm{u}_\beta)\\ &\quad\times\Big(|\nabla_{\alpha\beta}|^2+|\nabla_{\alpha\bar\beta}|^2\Big)\Big]\quad . \end{aligned}\tag{14}$$

A.1 Non–Relativistic Models

A.1.1 Spherical Symmetry

In spherical symmetry non–relativistic spinors are given by

$$\Psi_{\alpha\mathrm{j}\ell\mathrm{m}}(\mathbf{r})=\langle\mathbf{r}|\alpha\mathrm{j}\ell\mathrm{m}\rangle=\psi_{\alpha\mathrm{j}\ell}(\mathrm{r})\,\Omega_{\mathrm{j}\ell\mathrm{m}}(\vartheta,\phi)\tag{15}$$

where α is the principal quantum number, j the total angular momentum, ℓ the orbital angular momentum, and m the projection of the total angular momentum. $\psi_{\alpha\mathrm{j}\ell}$ is the radial wave function to be treated numerically, while the spinor spherical harmonics $\Omega_{\mathrm{j}\ell\mathrm{m}}$ [63] can be treated analytically. When calculating the c.m. correction (14)

$$\begin{aligned}\langle\mathbf{P}^2_{\mathrm{c.m.}}\rangle &= -\hbar^2\sum_{\alpha,\mathrm{j},\ell}\mathrm{v}^2_{\alpha\mathrm{j}\ell}\sum_{\mathrm{m}=-\mathrm{j}}^{+\mathrm{j}}\langle\alpha\mathrm{j}\ell\mathrm{m}|\Delta|\alpha\mathrm{j}\ell\mathrm{m}\rangle\\ &\quad-\hbar^2\sum_{\alpha,\beta,\mathrm{j},\mathrm{J},\ell,\mathrm{L}}\mathrm{v}_{\alpha\mathrm{j}\ell}\,\mathrm{v}_{\beta\mathrm{JL}}\,(\mathrm{v}_{\alpha\mathrm{j}\ell}\,\mathrm{v}_{\beta\mathrm{JL}}+\mathrm{u}_{\alpha\mathrm{j}\ell}\,\mathrm{u}_{\beta\mathrm{JL}})\\ &\quad\times\sum_{\mathrm{m}=-\mathrm{j}}^{+\mathrm{j}}\sum_{\mathrm{M}=-\mathrm{J}}^{+\mathrm{J}}\big|\langle\alpha\mathrm{j}\ell\mathrm{m}|\nabla|\beta\mathrm{JLM}\rangle\big|^2\end{aligned}\tag{16}$$

the summation over m and M can be performed analytically: the sum over m (for given j and ℓ) of the matrix elements of the Laplacian gives simply $2\mathrm{j}+1$ times the expectation value of the Laplacian of $\psi_{\alpha\mathrm{j}\ell}$, while the square of the matrix elements of the nabla operator reads

$$\begin{aligned}&\sum_{\mathrm{m}=-\mathrm{j}}^{+\mathrm{j}}\sum_{\mathrm{M}=-\mathrm{J}}^{+\mathrm{J}}\big|\langle\alpha\mathrm{j}\ell\mathrm{m}|\nabla|\beta\mathrm{JLM}\rangle\big|^2\\ &=(-1)^{\mathrm{L}+\ell}\,(2\mathrm{J}+1)\,(2\mathrm{j}+1)\begin{Bmatrix}\mathrm{J}&\mathrm{j}&1\\ \ell&\mathrm{L}&\frac{1}{2}\end{Bmatrix}^2\\ &\quad\times\big[\mathrm{L}\,\delta_{\ell,\mathrm{L}-1}\,\mathrm{A}_{\alpha\beta}\,\mathrm{B}_{\beta\alpha}+\ell\,\delta_{\mathrm{L},\ell-1}\,\mathrm{A}_{\beta\alpha}\,\mathrm{B}_{\alpha\beta}\big]\end{aligned}\tag{17}$$

with

$$\mathrm{A}_{\alpha\beta} = \int \mathrm{dr}\ \mathrm{r}^2\ \psi_{\alpha\mathrm{j}\ell}\left(\partial_\mathrm{r} + \tfrac{\mathrm{L}+1}{\mathrm{r}}\right)\psi_{\beta\mathrm{JL}} \quad ,$$
$$\mathrm{B}_{\alpha\beta} = \int \mathrm{dr}\ \mathrm{r}^2\ \psi_{\alpha\mathrm{j}\ell}\left(\partial_\mathrm{r} - \tfrac{\mathrm{L}}{\mathrm{r}}\right)\psi_{\beta\mathrm{JL}} \quad . \tag{18}$$

The square of the 6j symbol occurring in (17) is given by

$$\left\{\begin{array}{ccc}\mathrm{J} & \mathrm{j} & 1\\ \ell & \mathrm{L} & \frac{1}{2}\end{array}\right\}^2 = \frac{(\ell+\mathrm{J}+\frac{5}{2})(\ell+\mathrm{J}-\frac{1}{2})}{(2\mathrm{j}+1)(2\mathrm{J}+1)(2\ell+1)(2\mathrm{L}+1)} \times(\delta_{\mathrm{j},\ell+1}\,\delta_{\mathrm{J,L}+1} + \delta_{\mathrm{j},\ell-1}\,\delta_{\mathrm{J,L}-1}) + \frac{(\mathrm{J}-\ell+\frac{3}{2})(\ell-\mathrm{J}+\frac{3}{2})}{(2\mathrm{j}+1)(2\mathrm{J}+1)(2\ell+1)(2\mathrm{L}+1)} \times(\delta_{\mathrm{j},\ell+1}\,\delta_{\mathrm{J,L}-1} + \delta_{\mathrm{j},\ell-1}\,\delta_{\mathrm{J,L}+1}) \tag{19}$$

A.1.2 Axial Symmetry

Assuming axial symmetry, a spinor with angular momentum projection m is given by

$$\Psi_\alpha(\mathbf{r}) = \begin{pmatrix}\psi_\alpha^{(+)}(\mathrm{r},\mathrm{z})\ \exp\left[\mathrm{i}\left(\mathrm{m}-\frac{1}{2}\right)\phi\right]\\ \psi_\alpha^{(-)}(\mathrm{r},\mathrm{z})\ \exp\left[\mathrm{i}\left(\mathrm{m}+\frac{1}{2}\right)\phi\right]\end{pmatrix} \quad . \tag{20}$$

The $\psi_\alpha^{(\sigma)}$ can be chosen to be real. The matrix elements of the nabla operator needed to calculate (13) or (14) are given by

$$\begin{aligned}\nabla_{\alpha\beta}\cdot\nabla^*_{\alpha\beta} &= \delta_{\mathrm{m}_\alpha\mathrm{m}_\beta}\,\mathrm{A}_{\alpha\beta}\,\mathrm{A}_{\alpha\beta}\\ &\quad +\tfrac{1}{2}\left(\delta_{\mathrm{m}_\alpha,\mathrm{m}_\beta-1}\,\mathrm{B}^-_{\alpha\beta}\,\mathrm{B}^-_{\alpha\beta} + \delta_{\mathrm{m}_\alpha,\mathrm{m}_\beta+1}\,\mathrm{B}^+_{\alpha\beta}\,\mathrm{B}^+_{\alpha\beta}\right)\\ \nabla_{\alpha\beta}\cdot\nabla_{\bar\alpha\bar\beta} &= \delta_{\mathrm{m}_\alpha\mathrm{m}_\beta}\,\mathrm{A}_{\alpha\beta}\,\mathrm{A}_{\bar\alpha\bar\beta}\\ &\quad +\tfrac{1}{2}\left(\delta_{\mathrm{m}_\alpha,\mathrm{m}_\beta-1}\,\mathrm{B}^-_{\alpha\beta}\,\mathrm{B}^+_{\bar\alpha\bar\beta} + \delta_{\mathrm{m}_\alpha,\mathrm{m}_\beta+1}\,\mathrm{B}^+_{\alpha\beta}\,\mathrm{B}^-_{\bar\alpha\bar\beta}\right)\\ \nabla_{\alpha\bar\beta}\cdot\nabla^*_{\alpha\bar\beta} &= \tfrac{1}{2}\,\delta_{\mathrm{m}_\alpha,\frac{1}{2}}\,\delta_{\mathrm{m}_\beta,\frac{1}{2}}\,\mathrm{C}_{\alpha\beta}\,\mathrm{C}_{\alpha\beta}\end{aligned} \tag{21}$$

with

$$\mathrm{A}_{\alpha\beta} = \int \mathrm{d}^3\mathrm{r}\sum_{\sigma=\pm}\psi_\alpha^{(\sigma)}\,\partial_\mathrm{z}\,\psi_\beta^{(\sigma)} \tag{22}$$

$$\mathrm{B}^\pm_{\alpha\beta} = \int \mathrm{d}^3\mathrm{r}\sum_{\sigma=\pm}\psi_\alpha^{(\sigma)}\left(\partial_\mathrm{r} \pm \frac{\mathrm{m}_\beta - \frac{\sigma}{2}}{\mathrm{r}}\right)\psi_\beta^{(\sigma)} \tag{23}$$

$$\mathrm{C}_{\alpha\beta} = \int \mathrm{d}^3\mathrm{r}\sum_{\sigma=\pm}(-\sigma)\psi_\alpha^{(\sigma)}\left(\partial_\mathrm{r} + \frac{\mathrm{m}_\beta + \frac{\sigma}{2}}{\mathrm{r}}\right)\psi_\beta^{(-\sigma)} \tag{24}$$

where the volume element is given by $\mathrm{d}^3\mathrm{r} = 2\pi\,\mathrm{dr}\,\mathrm{r}\,\mathrm{dz}$.

A.1.3 Cartesian Representation

In Cartesian representation the non–relativistic spinors are given by

$$\Psi_\alpha(\mathbf{r}) = \begin{pmatrix}\psi_\alpha^{(++)}(\mathbf{r}) + \mathrm{i}\,\psi_\alpha^{(+-)}(\mathbf{r})\\ \psi_\alpha^{(-+)}(\mathbf{r}) + \mathrm{i}\,\psi_\alpha^{(--)}(\mathbf{r})\end{pmatrix} \quad , \tag{25}$$

where the $\psi_\alpha^{(\sigma\eta)}$ are real functions. The matrix elements of the nabla operator needed for the calculation of (13) are given by

$$\begin{aligned}\nabla_{\alpha\beta}\cdot\nabla^*_{\alpha\beta} &= \mathbf{A}^2_{\alpha\beta} + \mathbf{B}^2_{\alpha\beta}\\ \nabla_{\alpha\bar\beta}\cdot\nabla^*_{\alpha\bar\beta} &= \mathbf{A}^2_{\alpha\bar\beta} + \mathbf{B}^2_{\alpha\bar\beta}\end{aligned} \tag{26}$$

with

$$\begin{aligned}\mathrm{A}_{\alpha\beta} &= \int \mathrm{d}^3\mathrm{r}\sum_{\sigma,\eta}\psi_\alpha^{(\sigma\eta)}\,\nabla\,\psi_\beta^{(\sigma\eta)}\\ \mathrm{A}_{\alpha\bar\beta} &= \int \mathrm{d}^3\mathrm{r}\sum_{\sigma,\eta}\sigma\eta\,\psi_\alpha^{(-\sigma\eta)}\,\nabla\,\psi_\beta^{(\sigma\eta)}\\ \mathrm{B}_{\alpha\beta} &= \int \mathrm{d}^3\mathrm{r}\sum_{\sigma,\eta}\eta\,\psi_\alpha^{(\sigma-\eta)}\,\nabla\,\psi_\beta^{(\sigma\eta)}\\ \mathrm{B}_{\alpha\bar\beta} &= \int \mathrm{d}^3\mathrm{r}\sum_{\sigma,\eta}\sigma\,\psi_\alpha^{(-\sigma-\eta)}\,\nabla\,\psi_\beta^{(\sigma\eta)}\end{aligned} \tag{27}$$

A.2 Relativistic Models

Relativistic kinematics plays no role for nuclear ground states, the c.m. correction can be calculated in non–relativistic approximation in relativistic models. The main difference between relativistic and non–relativistic models is that the relativistic spinors have four components which changes the calculation of $\langle\hat{\mathbf{P}}^2_{\mathrm{c.m.}}\rangle$.

A.2.1 Spherical Symmetry

The relativistic spinors in spherical symmetry are given by

$$\Phi_{\alpha\kappa\mathrm{m}}(\mathbf{r}) = \langle\mathbf{r}|\alpha\kappa\mathrm{m}\rangle = \begin{pmatrix}\psi^{(+)}_{\alpha\kappa}(\mathrm{r})\,\Omega_{\kappa,\mathrm{m}}(\vartheta,\varphi)\\ \mathrm{i}\psi^{(-)}_{\alpha\kappa}(\mathrm{r})\,\Omega_{-\kappa,\mathrm{m}}(\vartheta,\varphi)\end{pmatrix} \tag{28}$$

The quantum number κ is related to the total and orbital angular momentum by $\mathrm{j} = |\kappa| - \frac{1}{2}$ and $\ell = \mathrm{j} + \frac{1}{2}\frac{\kappa}{|\kappa|}$. The real functions $\psi^{(\eta)}$ are the radial part of the upper and lower components of the wave functions, the $\Omega_{\kappa,\mathrm{m}}$ are spinor spherical harmonics [63] with angular momenta corresponding to κ. The variance of the total momentum is now given by

$$\begin{aligned}\langle\mathbf{P}^2_{\mathrm{c.m.}}\rangle &= -\hbar^2\sum_{\alpha,\kappa}\mathrm{v}^2_{\alpha\kappa}\sum_{\mathrm{m}=-\mathrm{j}}^{+\mathrm{j}}\langle\alpha\kappa\mathrm{m}|\Delta|\alpha\kappa\mathrm{m}\rangle\\ &\quad -\hbar^2\sum_{\alpha,\beta,\kappa\mathrm{K}}\mathrm{v}_{\alpha\kappa}\,\mathrm{v}_{\beta\mathrm{K}}\,(\mathrm{v}_{\alpha\kappa}\,\mathrm{v}_{\beta\mathrm{K}} + \mathrm{u}_{\alpha\kappa}\,\mathrm{u}_{\beta\mathrm{K}})\\ &\quad\times\sum_{\mathrm{m}=-\mathrm{j}}^{+\mathrm{j}}\sum_{\mathrm{M}=-\mathrm{J}}^{+\mathrm{J}}\left|\langle\alpha\kappa\mathrm{m}|\nabla|\beta\mathrm{KM}\rangle\right|^2\end{aligned} \tag{29}$$

with

$$\sum_{\mathrm{m}=-\mathrm{j}}^{+\mathrm{j}}\langle\alpha\kappa\mathrm{m}|\Delta|\alpha\kappa\mathrm{m}\rangle = (2\mathrm{j}+1)\sum_{\eta=\pm}\int\mathrm{dr}\,\mathrm{r}^2\,\psi^{(\eta)}_{\alpha\kappa}\,\Delta\,\psi^{(\eta)}_{\alpha\kappa} \tag{30}$$

and

$$\sum_{\mathrm{m}=-\mathrm{j}}^{+\mathrm{j}} \sum_{\mathrm{M}=-\mathrm{J}}^{+\mathrm{J}} \left|\langle \alpha \mathrm{j} \kappa | \nabla | \beta \mathrm{K M} \rangle\right|^2 \tag{31}$$
$$= (2\mathrm{J}+1)\,(2\mathrm{j}+1) \sum_{\eta=\pm} (-1)^{\mathrm{L}^{(\eta)}+\ell^{(\eta)}} \left\{ \begin{array}{ccc} \mathrm{J} & \mathrm{j} & 1 \\ \ell^{(\eta)} & \mathrm{L}^{(\eta)} & \frac{1}{2} \end{array} \right\}^2$$
$$\times \Big[\mathrm{L}\, \delta_{\ell^{(\eta)},\mathrm{L}^{(\eta)}-1}\, \mathrm{A}^{(\eta)}_{\alpha\beta}\, \mathrm{B}^{(\eta)}_{\beta\alpha} + \ell\, \delta_{\mathrm{L}^{(\eta)},\ell^{(\eta)}-1}\, \mathrm{A}^{(\eta)}_{\beta\alpha}\, \mathrm{B}^{(\eta)}_{\alpha\beta} \Big]$$

where A and B are given by

$$\mathrm{A}^{(\eta)}_{\alpha\beta} = \int \mathrm{d r}\ \mathrm{r}^2\ \psi_{\alpha\kappa} \left(\partial_\mathrm{r} + \tfrac{\mathrm{L}^{(\eta)}+1}{\mathrm{r}} \right) \psi_{\beta\mathrm{K}} \quad ,$$
$$\mathrm{B}^{(\eta)}_{\alpha\beta} = \int \mathrm{d r}\ \mathrm{r}^2\ \psi_{\alpha\kappa} \left(\partial_\mathrm{r} - \tfrac{\mathrm{L}^{(\eta)}}{\mathrm{r}} \right) \psi_{\beta\mathrm{K}} \quad . \tag{32}$$

The 6j symbol appearing in (31) is again given by (19).

A.2.2 Axial Symmetry

The relativistic spinors in axial symmetry are given by

$$\Phi_\alpha(\mathbf{r}) = \begin{pmatrix} \psi^{(++)}_\alpha(\mathrm{r},\mathrm{z})\ \exp\left[\mathrm{i}\left(\mathrm{m}-\frac{1}{2}\right)\phi\right] \\ \psi^{(+-)}_\alpha(\mathrm{r},\mathrm{z})\ \exp\left[\mathrm{i}\left(\mathrm{m}+\frac{1}{2}\right)\phi\right] \\ \mathrm{i}\,\psi^{(-+)}_\alpha(\mathrm{r},\mathrm{z})\ \exp\left[\mathrm{i}\left(\mathrm{m}-\frac{1}{2}\right)\phi\right] \\ \mathrm{i}\,\psi^{(--)}_\alpha(\mathrm{r},\mathrm{z})\ \exp\left[\mathrm{i}\left(\mathrm{m}+\frac{1}{2}\right)\phi\right] \end{pmatrix} \tag{33}$$

where $(\mathrm{r},\mathrm{z},\phi)$ are cylindrical coordinates and m is the projection of the total angular momentum. The $\psi^{(\eta\sigma)}$ are real functions, where η denotes upper and lower components and $\sigma/2$ the spin projection. The matrix elements entering (21) are now given by

$$\Delta_{\alpha\alpha} = \int \mathrm{d}^3\mathrm{r} \sum_{\eta,\sigma} \psi^{(\eta\sigma)}_\alpha \left[\partial^2_\mathrm{r} + \tfrac{1}{\mathrm{r}}\,\partial_\mathrm{r} - \frac{(\mathrm{m}-\frac{\sigma}{2})^2}{\mathrm{r}^2} + \partial^2_\mathrm{z} \right] \psi^{(\eta\sigma)}_\alpha$$
$$\mathrm{A}_{\alpha\beta} = \int \mathrm{d}^3\mathrm{r} \sum_{\eta,\sigma} \psi^{(\eta\sigma)}_\alpha\, \partial_\mathrm{z}\, \psi^{(\eta\sigma)}_\beta$$
$$\mathrm{B}^{\pm}_{\alpha\beta} = \int \mathrm{d}^3\mathrm{r} \sum_{\eta\sigma} \psi^{(\eta\sigma)}_\alpha \left(\partial_\mathrm{r} \pm \frac{\mathrm{m}_\beta - \frac{\sigma}{2}}{\mathrm{r}} \right) \psi^{(\eta\sigma)}_\beta$$
$$\mathrm{C}_{\alpha\beta} = \int \mathrm{d}^3\mathrm{r} \sum_{\eta\sigma} \eta\,\sigma\, \psi^{(\eta\sigma)}_\alpha \left(\partial_\mathrm{r} + \frac{\mathrm{m}_\beta + \frac{\sigma}{2}}{\mathrm{r}} \right) \psi^{(\eta,-\sigma)}_\beta \tag{34}$$

A.2.3 Cartesian Representation

The relativistic spinors in Cartesian representation are given by

$$\Phi_\alpha(\mathbf{r}) = \begin{pmatrix} \psi^{(+++)}_\alpha(\mathbf{r}) + \mathrm{i}\,\psi^{(++-)}_\alpha(\mathbf{r}) \\ \psi^{(+-+)}_\alpha(\mathbf{r}) + \mathrm{i}\,\psi^{(+--)}_\alpha(\mathbf{r}) \\ \psi^{(-++)}_\alpha(\mathbf{r}) + \mathrm{i}\,\psi^{(-+-)}_\alpha(\mathbf{r}) \\ \psi^{(--+)}_\alpha(\mathbf{r}) + \mathrm{i}\,\psi^{(---)}_\alpha(\mathbf{r}) \end{pmatrix} \tag{35}$$

where the $\psi^{(\eta\sigma\varrho)}_\alpha$ are real functions. η and σ have the same meaning as in the axial case, ϱ denotes real and imaginary part of a spinor component. The matrix elements of the Laplacian are given by

$$\Delta_{\alpha\alpha} = \int \mathrm{d}^3\mathrm{r} \sum_{\sigma,\eta,\varrho} \psi^{(\eta\sigma\varrho)}_\alpha\, \Delta\, \psi^{(\eta\sigma\varrho)}_\alpha \tag{36}$$

while the integrals needed to calculate the matrix elements of the nabla (26) are given by

$$\mathbf{A}_{\alpha\beta} = \int \mathrm{d}^3\mathrm{r} \sum_{\sigma,\eta,\varrho} \psi^{(\eta\sigma\varrho)}_\alpha\, \nabla\, \psi^{(\eta\sigma\varrho)}_\beta$$
$$\mathbf{A}_{\alpha\bar{\beta}} = \int \mathrm{d}^3\mathrm{r} \sum_{\sigma,\eta,\varrho} \psi^{(\eta,-\sigma,\varrho)}_\alpha\, \nabla\, \psi^{(\eta\sigma\varrho)}_\beta$$
$$\mathbf{B}_{\alpha\beta} = \int \mathrm{d}^3\mathrm{r} \sum_{\sigma,\eta,\varrho} \psi^{(\eta,\sigma,-\varrho)}_\alpha\, \nabla\, \psi^{(\eta\sigma\varrho)}_\beta$$
$$\mathbf{B}_{\alpha\bar{\beta}} = \int \mathrm{d}^3\mathrm{r} \sum_{\sigma,\eta,\varrho} \psi^{(\eta,-\sigma,-\varrho)}_\alpha\, \nabla\, \psi^{(\eta\sigma\varrho)}_\beta \tag{37}$$

References

1. P. Ring, P. Schuck, *The nuclear many–body problem* (Springer, New York, Heidelberg, Berlin, 1980)
2. K. W. Schmid, F. Grümmer, Rep. Prog. Phys. **50**, 731 (1987)
3. K. W. Schmid, and P.–G. Reinhard, Nucl. Phys. **A530**, 283 (1991)
4. J.–P. Blaizot, and G. Ripka, *Quantum Theory of Finite Systems* MIT Press, Cambridge (1986)
5. J. Friedrich, and P.–G. Reinhard, Phys. Rev. C **33**, 335 (1986)
6. P. Quentin, and H. Flocard, Ann. Rev. Nucl. Sci. **28**, 523 (1978)
7. P.–G. Reinhard, Rep. Prog. Phys. **52**, 439 (1989)
8. P. Ring, Prog. Part. Nucl. Phys. **37**, 193 (1996)
9. P.–G. Reinhard, and R. Y. Cusson, Nucl. Phys. **A378**, 418 (1982)
10. S. J. Krieger, P. Bonche, H. Flocard, P. Quentin, and M. S. Weiss, Nucl. Phys. **A517**, 275 (1990)
11. M. Bender, P.–G. Reinhard, K. Rutz, and J. A. Maruhn preprint, submitted to Phys. Rev. C (1999)
12. J. Dobaczewski, W. Nazarewicz, Phys. Rev. C **51**, R1070 (1995)
13. E. Chabanat, *Interactions effectives pour des conditions extrêmes d'isospin*, Université Claude Bernard Lyon–1, Thesis 1995, LYCEN T 9501, unpublished
14. E. Chabanat, P. Bonche, P. Haensel, J. Meyer, and R. Schaeffer, Nucl. Phys. **A635**, 231 (1998), **A643**, 441 (1998)
15. P.–G. Reinhard, M. Bender, K. Rutz, and J. A. Maruhn, Z. Phys. **A358**, 277 (1997)
16. P.–G. Reinhard and H. Flocard, Nucl. Phys. **A584**, 467 (1995)
17. M. Rufa, P.–G. Reinhard, J. A. Maruhn, W. Greiner, and M. R. Strayer, Phys. Rev. C **38**, 390 (1989)
18. M. Bender, K. Rutz, P.–G. Reinhard, J. A. Maruhn, and W. Greiner, Phys. Rev. C **60**, 034304 (1999)

19. P.–G. Reinhard, Z. Phys. **A329**, 257 (1988)
20. M. Beiner, H. Flocard, N. Van Giai, and P. Quentin, Nucl. Phys. **A238**, 29 (1975)
21. J. Bartel, P. Quentin, M. Brack, C. Guet, and H.–B. Håkansson, Nucl. Phys. **A386**, 79 (1982)
22. J. Dobaczewski, H. Flocard, and J. Treiner, Nucl. Phys. **A422**, 103 (1984)
23. F. Tondeur, M. Brack, M. Farine, and J. M. Pearson, Nucl. Phys. **A420**, 297 (1984)
24. J. M. Pearson, Y. Aboussir, A. K. Dutta, R. C. Nayak, M. Farine, F. Tondeur, Nucl. Phys. **A528**, 1 (1991)
25. J. Dechargé, and D. Gogny, Phys. Rev. **21**, 1568 (1980)
26. J.–F. Berger, M. Girod, and D. Gogny, Nucl. Phys. **A502**, 85c (1989)
27. M. M. Sharma, M. A. Nagarajan, and P. Ring, Phys. Lett. **B 312**, 377 (1993)
28. Y. Sugahara, and H. Toki, Nucl. Phys. **A579**, 557 (1994)
29. G. A. Lalazissis, J. König, and P. Ring, Phys. Rev. C **55**, 540 (1997)
30. P.–G. Reinhard, M. Rufa, J. A. Maruhn, W. Greiner, and J. Friedrich, Z. Phys. **A323**, 13 (1986)
31. M. N. Butler, D. W. L. Sprung, and J. Martorell, Nucl. Phys. **A422**, 157 (1984)
32. P.–G. Reinhard, *The Skyrme Hartree–Fock Model of the Nuclear Ground State*, in K. Langanke, J. A. Maruhn, S. E. Koonin [edts.], *Computational Nuclear Physics 1 – Nuclear Structure*, Springer, Berlin, Heidelberg, New York, 1991
33. R. W. Hasse, and W. D. Myers, *Geometrical Relationships of Macroscopic Nuclear Physics*, Springer, Berlin, 1988
34. S. Ćwiok, J. Dobaczewski, P.–H. Heenen, P. Magierski, and W. Nazarewicz, Nucl. Phys. **A611**, 211 (1996)
35. P.–H. Heenen, J. Dobaczewski, W. Nazarewicz, P. Bonche, and T. L. Khoo, Phys. Rev. C **57**, 1719 (1998)
36. G. A. Lalazissis, and P. Ring, Phys. Lett. **B427**, 225 (1998)
37. S. Takahara, N. Tajima, N. Onishi, Nucl. Phys. **A642**, 461 (1998)
38. P.–G. Reinhard, D. J. Dean, J. Dobaczewski, W. Nazarewicz, J. A. Maruhn, and M. R. Strayer, Phys. Rev. C **60**, 014302 (1999)
39. M. Brack, C. Guet, H.–B. Håkansson, Phys. Rep. **123**, 275 (1985)
40. J.–P. Blaizot, J. F. Berger, J. Dechargé, and M. Girod, Nucl. Phys. **A591**, 435 (1995)
41. E. Chabanat, P. Bonche, P. Haensel, J. Meyer, and R. Schaeffer, Nucl. Phys. **A627**, 710 (1997)
42. M. Farine, J. Côté, and J. M. Pearson, Phys. Rev. C **24**, 303 (1981)
43. J. M. Pearson, M. Farine, and J. Côté, Phys. Rev. C **26**, 267 (1982)
44. M. Farine, J. Côté, and J. M. Pearson, W. Stocker, Z. Phys. **A309**, 151 (1982)
45. M. Farine, and J. M. Pearson, Nucl. Phys. **A422**, 1 (1984)
46. M. Farine, J. M. Pearson, and F. Tondeur, Nucl. Phys. **A615**, 135 (1997)
47. M. Centelles, and X. Viñas, Nucl. Phys. **A563**, 173 (1993)
48. M. Centelles, X. Viñas, M. Barranco, and P. Schuck, Ann. Phys. (N.Y.) **221**, 165 (1993)
49. M. Del Estal, M. Centelles, and X. Viñas, Phys. Rev. C **56**, 1774 (1997)
50. C. Speicher, R. M. Dreizler, and E. Engel, Nucl. Phys. **A562**, 569 (1993)
51. D. Von Eiff, J. M. Pearson, W. Stocker, and M. K. Weigel, Phys. Lett. **B324**, 279 (1994)
52. D. Von Eiff, W. Stocker, and M. K. Weigel, Phys. Rev. C **50**, 1436 (1994)
53. W. Stocker, and T. v. Chossy, Phys. Rev. **C58**, 2777 (1998)
54. M. Del Estal, M. Centelles, and X. Viñas, Nucl. Phys. **A650**, 443 (1999)
55. M. Brack, private communication
56. H. Flocard, P. Quentin, D. Vautherin, M. Véneroni, and A. K. Kerman, Nucl. Phys. **A231**, 176 (1974)
57. M. Girod, and B. Grammaticos, Phys. Rev. **C27**, 2317 (1983)
58. V. Blum, J. A. Maruhn, P.–G. Reinhard, and W. Greiner, Phys. Lett. **B323**, 262 (1994)
59. K. Rutz, J. A. Maruhn, P.–G. Reinhard, and W. Greiner, Nucl. Phys. **A590**, 680 (1995)
60. P.–G. Reinhard, K. Goeke, Rep. Prog. Phys. **50**, 1 (1987)
61. J. N. Urbano, K. Goeke, P.–G. Reinhard, Nucl. Phys. **A370**, 329 (1981)
62. J. M. Eisenberg, and W. Greiner, *Nuclear Theory Vol I: Nuclear Models*, North–Holland, Amsterdam, 1987
63. D. A. Varshalovich, A. N. Moskalev, V. K. Khersonskii, *Quantum theory of angular momentum*, World Scientific, Singapore, 1988